

X-RAY WARM ABSORPTION AND EMISSION IN THE POLAR SCATTERED SEYFERT 1 GALAXY MRK 704

SIBASISH LAHA¹, GULAB C. DEWANGAN¹, AJIT K. KEMBHAVI¹
Accepted for publication in ApJ

ABSTRACT

We present a detailed study of the ionised environment of the Seyfert 1 galaxy Mrk 704 using medium and high resolution X-ray spectra obtained with a long *XMM-Newton* observation. The 0.3 – 10 keV continuum, well described by a power-law ($\Gamma \approx 1.86$) and two blackbodies ($kT \approx 0.085$ and 0.22 keV), is found to be affected by a neutral partial covering absorption ($N_H \approx 10^{23} \text{ cm}^{-2}$, covering fraction ≈ 0.22) and two warm absorber components. We identify a low ionisation, $\xi \sim 20 \text{ erg cm s}^{-1}$, and high outflow velocity, $v \sim 1350 \text{ km s}^{-1}$, phase producing the O VI and Fe M-shell unresolved-transition array (UTA). An additional high ionisation warm absorbing phase with $\xi \sim 500 \text{ erg cm s}^{-1}$ and low outflow velocity, $v \sim 540 \text{ km s}^{-1}$, gives rise to absorption features due to O VII, O VIII, N VI, N VII and C VI. We also detected weak emission lines of He-like triplets from O VII and N VI ions, thus making Mrk 704 a Seyfert 1 galaxy with both warm absorption and emission. The emission lines are well described by two warm emitting, photoionised media with different densities but comparable ξ , suggesting discrete clouds of warm emission. The high density phase ($n_e \sim 10^{13} \text{ cm}^{-3}$) responsible for the resonance lines appears to outflow at high velocity $\sim 5000 \text{ km s}^{-1}$. The low velocity, low density phase is likely similar to the X-ray line emitting regions found in Seyfert 2 galaxies. The physical conditions of warm emitters and warm absorbers suggest that these clouds are similar but observed in absorption along our line of sight and in emission at other lines of sight. The unique line of sight passing close to the torus opening angle is likely responsible for the neutral partial covering absorption and our view of emission lines due to the suppressed continuum in this polar scattered Seyfert 1 galaxy.

Subject headings: Active galaxies, Warm absorbers, Warm emitters, X-rays

1. INTRODUCTION

It is well known that the 0.1 – 10 keV spectra of many Active Galactic Nuclei (AGN) are modified by partially ionised material along our line of sight and intrinsic to the source. Such X-ray absorbing clouds which significantly affect the observed X-ray spectrum have been named the “partially ionised absorber” or the “warm absorber” (Halpern 1984). The availability of high resolution grating X-ray spectra with *XMM-Newton* and *Chandra* have greatly improved our understanding of discrete absorption and emission features from AGN.

Earlier studies on Seyfert galaxies by Blustin et al. (2005) and Piconcelli et al. (2005) revealed that around half of the type 1 objects show signatures of warm absorption in their X-ray spectra. These warm absorbers give rise to narrow absorption lines and edges, from elements at a wide range of ionisation stages (see e.g., Kaastra et al. (2000); Kaspi et al. (2000a); Blustin et al. (2005)). The most prominent of the absorption features are from the H-like and He-like ions of C, N, O, Ne and lower ionisation states of Fe. For example O VII (0.74 keV), O VIII (0.87 keV), Ne X (1.36 keV) and Fe (UTA at ~ 0.7 keV) are primary absorbers above 0.5 keV while C V (0.39 keV) and C VI (0.49 keV) dominate for energies below it (Halpern 1984; Nandra & Pounds 1994; Reynolds 1997; George et al. 1998). These lines and edges are sensitive diagnostics of the ionisation structure and kinematics of the gas.

The measured blueshift of the absorption lines with respect to the systemic velocity imply that these absorbers

are outflowing with moderate velocities in the range of $\sim 100 - 1000 \text{ km s}^{-1}$. In some AGNs, high velocity outflows have also been detected (e.g., Reeves et al. 2003; Dadina & Cappi 2004; Dasgupta et al. 2005; Braitto et al. 2007). The resulting mass outflow rate can be a substantial fraction of the accretion rate required to power the AGN. Thus, warm absorbers can be dynamically important and the knowledge of their state, location, geometry and dynamics would help in understanding the central engines of AGN (Mathur et al. 1995).

We expect the warm absorbers also to emit in soft X-rays (Netzer 1993). However, most Seyfert 1s do not show clear evidence for such warm emission lines. This may be due to our direct view of the central power source. According to the Unified Model of AGN, Seyfert 1s are those in which the continuum emitted from the central engine is viewed directly. This continuum flux being orders of magnitude greater than the emission line fluxes the latter is not detectable even though it may be present. On the other hand, the primary continuum from Seyfert 2s is obscured by an optically thick torus and the narrow emission lines in the soft X-rays are detectable on top of an attenuated weak X-ray continuum. In their detailed study of the emission line spectrum of the Seyfert 2 galaxy NGC 1068, Kinkhabwala et al. (2002) have shown that the emission lines arise from clouds with a large range in ionisation parameters and column densities, typical of warm absorbers. This suggests that the emission line spectrum of NGC 1068 arises from clouds that would be observed as warm absorbers if the source were a Seyfert 1 galaxy.

The orientation of some AGNs is intermediate between Seyfert 1 and 2. That is, they are viewed with an inclina-

¹ Inter University Centre for Astronomy and Astrophysics; email: laha@iucaa.ernet.in ; gulabd@iucaa.ernet.in

tion comparable with the “torus” opening angle, hence the line of sight to the nucleus passes through the upper layers of the torus. The emission from the central engine therefore suffers only a moderate extinction through the torus rim (Smith et al. 2002), and their polarised spectra are dominated by polar scattering. Such an AGN is called a polar scattered Seyfert 1 (PSS) galaxy. In their detailed study of the optical polarisation spectra of Seyfert 1 nuclei, Smith et al. have found a sample of such sources. They have shown that such AGN exhibit polarised broad emission lines, characteristic of a Seyfert 2 as well as Seyfert 1 spectra in total light. These objects are of particular interest in the context of the unification scheme since they define a critical viewing angle at which both Seyfert 1 and Seyfert 2 characteristics are manifested in the spectrum. Due to their unique viewing angles, PSS galaxies are expected to show interesting absorption and emission features. It is this unique viewing angle that led us to perform a detailed study of the nuclear environment of a PSS galaxy.

Mrk 704 is a PSS galaxy (Smith et al. 2004) and is located at $z = 0.0292$. It is a high Galactic latitude bright X-ray source, detected with *ROSAT* (Schwope et al. 2000). It has also been detected with *ASCA*, *Swift* XRT and BAT. Ajello et al. (2008) have modeled the *ASCA* and *Swift* XRT & BAT spectral data with a partial covering absorption model (covering fraction ~ 0.5 and a high column density $N_{\text{H}} \sim 1.5 \times 10^{23} \text{ cm}^{-2}$) modifying a power-law with $\Gamma \sim 1.36$. They also detected an iron line with an equivalent width of 160 eV. As a part of systematic study of a sample Jiménez-Bailón et al. (2008) have studied the RGS spectra of Mrk 704 obtained from a short (~ 25 ks) *XMM-Newton* observation and found two distinct components of warm absorbers. Here, we perform a detailed X-ray spectral study of Mrk 704, both medium and high resolution, based on a long ~ 100 ks *XMM-Newton* observation.

The paper is organised as follows. We describe the observation and data reduction in Section 2 and spectral analysis and modeling in Section 3. We discuss our results in Section 4, followed by a summary in Section 5. Throughout this work we have used the cosmological parameters $H_0 = 71 \text{ km s}^{-1} \text{ Mpc}^{-1}$, $\Omega_m = 0.27$, $\Omega_\Lambda = 0.73$ to calculate distance.

2. OBSERVATION AND DATA REDUCTION

We used archival data on Mrk 704 which was observed by *XMM-Newton* on 2nd November 2008 (obsID:0502091601) for a total exposure of 98.2 ks. The EPIC-pn and MOS cameras were operated in the small window mode using the thin filter. The data were processed using SAS version 9 and the latest calibration database as available on 17th January 2010.

The data were first filtered using the standard filtering criterion. Examination of the background rate above 10 keV showed that the observation was partly affected by a flaring particle background after an elapsed time of ~ 87 ks and this later period was therefore excluded to improve the signal-to-noise-ratio. We checked the photon pile-up using the SAS task *epatplot* and found that there were no noticeable pile-up in either EPIC-pn or MOS data. We quote results based on EPIC-pn data due to its higher signal-to-noise compared to the MOS data. We have used the good X-ray events (FLAG=0),

pattern ≤ 4 . To extract the source spectrum we used a circular region of 45 arcsec, centred on the centroid of the source. We extracted the background spectrum from appropriate nearby circular regions, free of sources. We created the ancillary response file (ARF) and the redistribution matrix file (RMF) using the SAS tasks *arfgen* and *rmfgen*.

We processed the RGS data using the SAS task *rgsproc*. We assessed the background through examination of the light curve. We chose a region, CCD9, that is most susceptible to proton events and generally records the least source events due to its location close to the optical axis and extracted the background light curve. We then generated a good time interval file to filter the eventlist and extracted the first order source and background spectrum. The response matrices were generated using the task *rgsrmfgen*.

3. SPECTRAL ANALYSIS

We used the Interactive Spectral Interpretation System (ISIS) version 1.5.0-20 for our spectral fitting. All uncertainties quoted are 90% for one parameter of interest unless otherwise noted.

3.1. The 0.3 – 10 keV EPIC-pn spectrum

We begin with the spectral analysis of the broadband (0.3 – 10 keV) EPIC-pn spectral data. We grouped the EPIC-pn data to a minimum of 300 counts per bin and used the χ^2 statistics. A single absorbed power-law model resulted in a poor fit to the pn data, providing a minimum $\chi^2 = 11954$ for 559 degrees of freedom (dof). We therefore fitted the 2 – 10 keV data which was devoid of any soft excess, with an absorbed power-law model.

The simple power-law model with absorption due to neutral hydrogen column in our Galaxy (*wabs*) provided a $\chi^2/\text{dof} = 361/219$. The best fit neutral absorption column density $N_{\text{H}} \leq 3.4 \times 10^{20} \text{ cm}^{-2}$ is consistent with Galactic column ($N_{\text{H}}^{\text{G}} = 2.97 \times 10^{20} \text{ cm}^{-2}$, Kalberla et al. (2005)). So we fixed N_{H} to this value. Previous studies on this source found strong intrinsic cold absorption (Ajello et al. (2008)). We tested for the presence of intrinsic cold absorption by using the (*zwabs*) component at the source redshift and found that the fit statistics did not improve, thus implying the absence of a fully covering intrinsic cold absorption. We then tested for the presence of partial covering cold absorption by using the (*zpcfabs*) model component. The fit improved by $\Delta\chi^2 = 64$ for two extra parameters. The best fit intrinsic neutral absorption column density is $N_{\text{H}} = 41_{-8}^{+7} \times 10^{22} \text{ cm}^{-2}$ and covering fraction is $0.18_{-0.08}^{+0.04}$. Examination of the residuals showed a prominent FeK α line at ~ 6.4 keV. Addition of a Gaussian line profile improved the fit by $\Delta\chi^2 = 124$ for three additional parameters, providing a statistically acceptable fit. The best-fit parameters are: the photon index $\Gamma = 1.88 \pm 0.01$, iron line centroid $E_{\text{FeK}\alpha} = 6.39 \pm 0.03$ keV, width $\sigma = 0.10_{-0.03}^{+0.03}$ keV and an equivalent width, $EW = 125 \pm 3$ eV. The FWHM of the line corresponds to a velocity $v_{\text{FWHM}} \approx 11000 \text{ km s}^{-1}$ which indicates that the line may originate from inner broadline region or the accretion disc. We also fit the line using *diskline* model which signifies line emission from a rotating disc. The best fit *diskline* parameters are $E_{\text{FeK}\alpha} = 6.36 \pm 0.03$ keV, $\text{norm} = 2.58_{-0.50}^{+0.62} \times$

10^{-5} photons $\text{cm}^{-2} \text{s}^{-1}$, the inner and outer radius $R_{in} = 10r_g$, $R_{out} = 21000r_g$ ($r_g = GM_{BH}/c^2$ is the gravitational radius), emissivity index $\beta = -1.85$ and an inclination of 42.9 degrees. The observed 2 – 10 keV flux is $1.10^{+0.011}_{-0.012} \times 10^{-11} \text{ erg cm}^{-2} \text{ s}^{-1}$ corresponding to a luminosity $L_X = 2.18^{+0.02}_{-0.02} \times 10^{42} \text{ erg s}^{-1}$.

We extrapolated the best-fit 2 – 10 keV model (`wabs` \times `zpcfabs` \times `(powerlaw+gaussian)`) to the soft X-ray band (0.3 – 2 keV) and found that there is a huge soft excess below 2 keV. Figure 1 panel (f) shows the presence of soft excess over an absorbed power-law. The origin of soft excess in type 1 AGNs is still unclear. Several models such as single or multiple black-bodies, multicolor disk black-body, blurred reflection from partially ionised material, smeared absorption, and thermal Comptonization in an optically thick medium can provide statistically good fit to the observed soft excess (Magdziarz et al. 1998; Fabian et al. 2002; Gierliński & Done 2004; Dewangan et al. 2007). Since we are mainly interested with the absorption phenomenon, any of the above models will serve our purpose to characterise the continuum in the soft X-ray band (0.3 – 2 keV). We have used the simple black-body (`bbody`) to describe the soft excess emission. We added the `bbody` component to the absorbed power-law plus Gaussian line model and performed the fitting in the 0.3 – 10 keV band. This fit resulted in an improvement, $\Delta\chi^2 = 2400$ for 2 extra parameters, compared to the absorbed power-law + Gaussian line model which was $\chi^2/\text{dof} = 3659/554$. The black-body temperature is $kT = 0.085 \pm 0.002$ keV. The best-fit model is not statistically acceptable. So we further used one more `bbody` and found an improvement in the fit by $\Delta\chi^2 = 380$ for two extra parameters. The second black-body temperature is $kT = 0.22 \pm 0.02$ keV.

Examination of the residuals showed broad absorption features in the 0.5 – 1 keV region (see Fig. 1, panel (d)). The absorption features likely include the O VII absorption edge and Fe-M shell Unresolved Transition Arrays (UTA), which are the typical signatures of warm absorbers. Therefore, we created warm absorber table model `mtable` using CLOUDY to fit those absorption features.

3.2. Cloudy modelling

We created the model for warm absorption using the photoionisation simulation code CLOUDY (version 08.00, last described by Ferland et al. (1998)). CLOUDY uses an extensive atomic database to predict the absorption and emission spectrum from a cloud. The clouds are assumed to have a uniform spherical distribution around the central source and are photoionised by the source. CLOUDY performs the simulations by dividing the surrounding medium into thin concentric shells referred to as zones. The thickness of the zones are chosen small enough for the physical conditions across them to be nearly constant. For each zone the simulations are carried out by simultaneously solving the equations that balance ionisation-neutralisation processes and heating-cooling processes. The model predicts the absorptions and emissions from such clouds in thermal and ionisation equilibrium.

We used an ionizing continuum of the central source that is typical of AGNs and closely matches with the

observed continuum in the X-ray band. This continuum is a power-law in the 1 eV – 100 keV band, and another steeper power-law in the UV whose upper exponential cutoff is parametrised with a temperature T_{BB} and the lower infrared cut off by T_{IR} . The continuum is expressed as

$$f_\nu = \nu^{\alpha_{uv}} \exp(-h\nu/kT_{BB}) \exp(-kT_{IR}/h\nu) + \eta\nu^{\alpha_x}, \quad (1)$$

where the coefficient η is the relative normalisation between the X-ray and the UV flux. It is calculated to produce the correct α_{ox} for the case where the Big Bump does not contribute to the emission at 2 keV and above. Here α_{ox} is defined as the slope of a nominal power-law connecting the continuum from 2500 Å and 2 keV, and is given by $\alpha_{ox} = 0.385 \log \left[\frac{f_\nu(2500\text{Å})}{f_\nu(2\text{keV})} \right]$ (Tananbaum et al.

1979). The X-ray power-law is only added for energies greater than 0.1 Rydbergs to prevent it from extending into the infrared, where a power-law of this slope would produce very strong free-free heating. The Big Bump component is assumed to have an infrared exponential cutoff at $kT_{IR} = 0.01$ Rydbergs. The free parameters in this model are T_{BB} , α_x , α_{ox} , α_{uv} .

The ionizing continuum to be used in CLOUDY should represent the true continuum of Mrk 704. We used the best-fit continuum model parameters derived from the broad-band EPIC-pn data. However, the continuum parameters, derived without modeling the warm absorption features, can be affected by the presence of warm absorber components. Therefore we followed an iterative procedure. In the first step, we obtained the X-ray continuum from the EPIC-pn best-fit model without the warm absorbers. We used this X-ray continuum and developed a CLOUDY warm absorber model. We fitted the broad band EPIC-pn spectrum with this CLOUDY warm absorber model and obtained new best-fit continuum parameters. In the second step we use the new best-fit continuum parameters to create a more realistic warm absorber model in CLOUDY. Finally we used this new warm absorber model to fit the EPIC-pn spectrum.

We have obtained the best fit EPIC-pn continuum parameters without the warm absorbers. In the first step we use them to model the warm absorbers using CLOUDY. The parameter values are $T_{BB} = 9.8 \times 10^5$ K (~ 0.085 keV), describing the soft-excess and $\alpha_x = -0.88$, describing the X-ray powerlaw as derived from the X-ray spectral fitting. The other parameter values were obtained from radio-quiet AGN studies $\alpha_{ox} = -1.4$ (Zamorani et al. 1981; Young et al. 2009) and $\alpha_{uv} = -0.5$ (Elvis et al. 1994).

The CLOUDY table model was built using the methods described in Porter et al. (2006). We varied $\log \xi$ and $\log N_H$ from -3 to +3 and 18 to 24, respectively, and created a multiplicative table model for the warm absorption. The electron density assumed was typical of BLR density $\sim 10^9 \text{ cm}^{-3}$. The table model was subsequently imported to the ISIS package.

First we used a single `mtable` component to model the absorption features. The model `wabs` \times `zpcfabs` \times `mtable` \times `(bbody(1)+bbody(2) + powerlaw + gaussian)` improved the fit ($\chi^2/\text{dof} = 876/550$) by $\Delta\chi^2 = 270$ for 3 extra parameters compared to the model without the warm absorber component. The

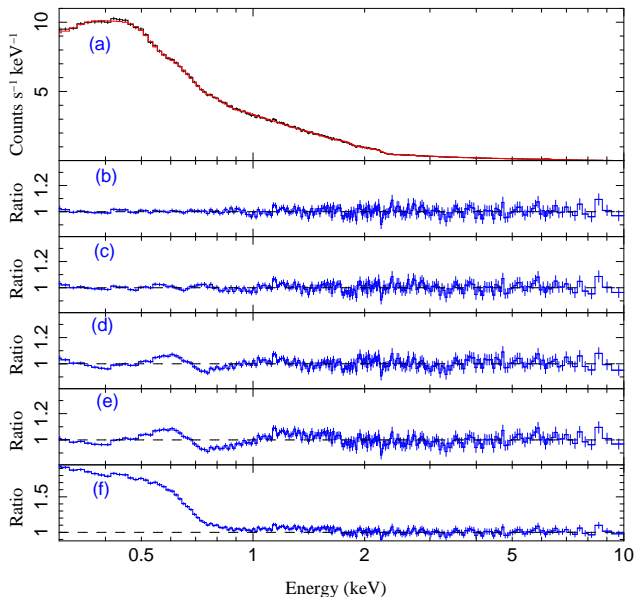


FIG. 1.— The figure shows the improvement of the fit to EPIC-pn data on addition of different model components. The panel (a) shows the observed EPIC-pn data and the best fit model. The lower panels show the ratio of the data and the respective models. The panel (f) shows the presence of soft excess over a power-law. The panels (e) and (d) show the improvement in fit upon addition of a black-body component each of temperature 0.1 keV and 0.25 keV respectively. The panels (c) and (b) show the improvement in fit on addition of a warm absorber component each of $\log \xi = 2.97$ and $\log \xi = 0.84$ respectively. Panel (b) also has a gaussian line in the soft X-ray. See Table 4 for details.

best fit parameters are $\log \xi = 0.99^{+0.13}_{-0.12}$ and $N_{\text{H}}^{\text{WA}} = 1.1^{+0.12}_{-0.15} \times 10^{21} \text{ cm}^{-2}$. Further inspection of the residuals at low energies showed additional absorption features in the 0.5 – 1 keV range that were not well described by the single warm absorber model. Therefore we used another *mtable* component. The second component further improved the fit by $\Delta\chi^2 = 40$ for 3 extra parameters resulting in $\chi^2/\text{dof} = 566/544$. The best fit values of the parameters are $\log \xi = 3.09 \pm 0.11$, $N_{\text{H}}^{\text{WA}} = 1 \pm 0.13 \times 10^{20} \text{ cm}^{-2}$ for the first component and $\log \xi = 0.88^{+0.08}_{-0.13}$, $N_{\text{H}}^{\text{WA}} = 1.0 \pm 0.11 \times 10^{21} \text{ cm}^{-2}$ for the second component. The power-law photon index is $\Gamma = 1.865 \pm 0.055$. We also tested the presence of a third warm absorber component but found no significant improvement and hence we excluded this third component from the analysis.

Now we have the new best-fit continuum parameters obtained from the continuum and warm absorber model fits to the EPIC-pn data, we used the new continuum to create more realistic warm absorption table model in CLOUDY. We use this realistic CLOUDY *mtable* model to fit the absorption features. The model `wabs × mtable × (bbody(1)+ bbody(2) + powerlaw + gaussian)` improved the fit ($\chi^2/\text{dof} = 876/550$) by $\Delta\chi^2 = 270$ for 3 extra parameters compared to the model without the warm absorber component. The best fit parameters are $\log \xi = 0.99^{+0.13}_{-0.12}$ and $N_{\text{H}}^{\text{WA}} = 1.1 \pm 0.15 \times 10^{20} \text{ cm}^{-2}$. Further inspection of the residuals at low energies showed additional absorption features in the 0.5 – 1 keV range that were not well described by

the single warm absorber model (see Fig. 1, panel(c)). Therefore we used another *mtable* component. The second component further improved the fit by $\Delta\chi^2 = 36$ for 3 extra parameters resulting in $\chi^2/\text{dof} = 570/544$. The best fit values of the parameters are $\log \xi = 2.97 \pm 0.11$, $N_{\text{H}}^{\text{WA}} = 1^{+0.4}_{-0.11} \times 10^{20} \text{ cm}^{-2}$ for the first component and $\log \xi = 0.84^{+0.25}_{-0.12}$, $N_{\text{H}}^{\text{WA}} = 9.7^{+1.3}_{-1.7} \times 10^{20} \text{ cm}^{-2}$ for the second component.

In the soft X-ray range we found some positive residuals which could be the signature of an emission feature. We used a Gaussian line to the model the emission feature which improved the fit by $\Delta\chi^2 = 11$ for two extra parameters. The Gaussian line $E = 0.565^{+0.008}_{-0.009} \text{ keV}$, flux = $1^{+0.4}_{-0.11} \times 10^{-4} \text{ photons cm}^{-2} \text{ s}^{-1}$, and the $\sigma = 0.01 \text{ keV}$. This unresolved line may be the OVII triplets. The observed data, the best-fit two component warm absorbed model and residuals are plotted in Fig. 1, panels (a) and (b). The total unabsorbed luminosity in 0.3-10 keV $L_{\text{X}} = 7^{+0.1}_{-0.06} \times 10^{42} \text{ erg s}^{-1}$. The power-law luminosity and the soft-excess luminosities in the same band are $L_{\text{X}} = 5.2^{+0.08}_{-0.05} \times 10^{42} \text{ erg s}^{-1}$ and $L_{\text{X}} = 1.78^{+0.02}_{-0.02} \times 10^{42} \text{ erg s}^{-1}$, respectively. The blackbody with $kT = 0.085 \text{ keV}$ has a luminosity of $L_{\text{X}} = 1.28^{+0.03}_{-0.03} \times 10^{42} \text{ erg s}^{-1}$ and the blackbody with $kT = 0.22 \text{ keV}$ has a luminosity $L_{\text{X}} = 4.8^{+0.12}_{-0.25} \times 10^{41} \text{ erg s}^{-1}$. We list the best fit parameters in Table 4. Due to the moderate spectral resolution, individual narrow absorption and/or emission features are not identified in the EPIC-pn data. However, the high resolution spectra obtained are well suited for a detailed study of the warm absorption and emission. Therefore, we have performed a detailed spectral analysis of the RGS data.

3.3. RGS spectroscopy

We grouped the RGS1 and RGS2 spectral data by a factor of two to ensure that each bin has non-zero counts. We used *C Statistics* (Cash 1979) for analysing the RGS data as the χ^2 statistics is not applicable in the case of low count data.

Both the RGS instruments operate in the 0.35 – 2.5 keV band with one CCD inoperative in each case. We compared the RGS1 and RGS2 data and found the two datasets agree well except near 11.5 Å. There was an emission feature at 11.5 Å in the RGS2 data which was not present in the RGS1 data. This is likely an instrumental feature and therefore we excluded the 11.3 – 11.7 Å region from the RGS2 data and performed joint fitting of RGS1 and RGS2 data in the 7 – 38 Å band.

The presence of strong warm absorption features became more evident in the high resolution RGS spectrum. We used a continuum model similar to that inferred from the EPIC-pn data, i.e., the sum of a power-law with $\Gamma = 1.865$ and two black-bodies with $kT = 0.085 \text{ keV}$ and 0.22 keV respectively. However we found that two black-bodies are statistically not necessary in the RGS spectrum. The higher temperature black-body has a low normalisation and hence does not improve the statistics.

The continuum is best modelled by an absorbed power-law and a single black-body. The power-law photon index and the intrinsic neutral absorption component parameters were fixed to the best fit EPIC-pn values since

TABLE 1
 DETAILS OF THE MODELLING OF THE EMISSION LINES IN RGS SPECTRA

Gaussian component	Rest energy (keV)	observed Energy (keV)	outflow velocity (km s ⁻¹)	Line flux photons cm ⁻² s ⁻¹	σ (eV)	EW (eV)	(ΔC) ^a	Ftest confidence
O VII(r)	0.574	0.5669 ^{+0.0015} _{-0.0014}	5041 ⁺⁶⁴⁰ ₋₆₄₀	3.86 ^{+1.03} _{-2.28} × 10 ⁻⁵	1.3 ^{+1.8} _{-0.09}	1.47 ^{+1.22} _{-0.79}	12	99 %
O VII(i)	0.568	0.553 ^{+0.004} _{-0.006}	777 ⁺²¹¹³ ₋₃₁₆₉	2.83 ^{+30.17} _{-1.36} × 10 ⁻⁵	0.9 ⁺¹ _{-0.9}	1.23 ^{+1.23} _{-0.59}	12	99%
O VII (f)	0.561	0.5449 ^{+0.0012} _{-0.0012}	90 ⁺⁵⁰⁰ ₋₅₀₀	5.42 ^{+4.5} _{-2.16} × 10 ⁻⁵	0.9 ⁺¹ _{-0.9}	2.4 ^{+1.8} _{-1.25}	10	98%
N VI(r)**	0.431	0.427 ^{+0.0007} _{-0.0012}	6300 ⁺⁴⁸⁷ ₋₈₃₅	1.7 ^{+1.1} _{-1.2} × 10 ⁻⁵	1 ^{+0.9} _{-0.8}	0.51 ^{+0.65} _{-0.40}	6	89%
N VI(i)**	0.426	0.4142 ^{+0.0011} _{-0.0012}	249 ± 704	< 2.17 × 10 ⁻⁵	0.25 ^{+0.25} _{-0.25}	—	—	—
N VI(f)	0.420	0.4085 ^{+0.0005} _{-0.0005}	485 ⁺³⁵⁷ ₋₃₅₇	2.30 ^{+1.9} _{-2.1} × 10 ⁻⁵	0.35 ^{+1.8} _{-0.35}	0.65 ^{+0.56} _{-0.44}	6	89%
C VI(Ly α)	0.367	0.3633 ^{+0.0013} _{-0.0021}	5670 ⁺⁸¹⁷ ₋₁₆₃₅	2.4 ^{+3.5} _{-1.8} × 10 ⁻⁵	0.5	0.49 ^{+0.71} _{-0.36}	5	83%

^a The ΔC improvement quoted for each Gaussian fit is for an addition of 3 parameters

All the parameters are obtained from simultaneous fit of RGS1 and RGS 2 data.

** These lines are only found in RGS1 data. Therefore during simultaneous fit we could only give the upper limit of the flux of N VI (i) emission line and it is consistent within the error ranges for the same line detected in RGS1 alone.

the RGS data alone cannot well constrain them. However the power-law normalisation and the `tbody` parameters were left to vary. The equivalent neutral hydrogen column density of the cold absorption was fixed to the Galactic value. On fitting the spectrum with a power-law, a black-body, the Galactic absorption and a partially covered neutral absorber we obtained a minimum $C = 3462$ with 3396 dof. The best-fit `tbody` temperature is $kT = 0.0835^{+0.0020}_{-0.0012}$ keV.

With the continuum model defined we applied the warm absorption model `mtable` and found an improvement in statistics by $\Delta C = 106$ for 3 additional parameters. A close inspection of the spectral residuals revealed further absorption features, seen as negative residuals in the 16–20 Å band. Hence we applied another component of the warm absorber. This second component further reduced the value of C by $\Delta C = 12$ for 3 additional parameters ($C/\text{dof} = 3344/3389$). The best-fit parameters are $\log \xi = 2.70^{+0.3}_{-0.15}$ and $N_{\text{H}}^{\text{WA}} = 2.69^{+1.11}_{-0.75} \times 10^{20} \text{ cm}^{-2}$ for the first component and $\log \xi = 1.27^{+0.27}_{-0.52}$ and $N_{\text{H}}^{\text{WA}} = 2 \pm 0.5 \times 10^{20} \text{ cm}^{-2}$ for the second component.

After fitting the data using two components of warm absorbers, we found emission lines as positive residuals in the spectra. There are two triplets in the wavelength ranges 22 – 23Å and 28 – 29Å. We fitted the individual emission lines with Gaussian line profiles. The best-fit line energies, widths and line fluxes are listed in Table 1. We compared the observed line energies and laboratory energies and identified them as the He-like triplet emission lines of O VII in the 22 – 23Å band and N VI triplets in the 28 – 29Å band. Such line triplets have also been detected in some of the Seyfert1 galaxies NGC 3783 (Behar et al. 2003), Mkn 335 (Longinotti et al. 2008), NGC 4051 (Pounds et al. 2004; Nucita et al. 2010). These are the three most intense lines of He-like ions: the *resonance* (w), *intercombination* ($x+y$), *forbidden* (z). They corre-

spond to transitions between $n=2$ and $n=1$ states which are close in wavelength:

1. *resonance* line (w : $1s^2S_0^1 - 1s2p P_1^1$),
2. *intercombination* lines (x,y : $1s^2S_0^1 - 1s2p P_{2,1}^3$)
3. *forbidden* line (z : $1s^2S_0^1 - 1s2s S_1^3$)

The two intercombination lines (x,y) are not resolved and detected as a single line in Mrk 704. The intercombination and the resonant line of the N VI triplet were not prominent in the RGS2 data. However the 1σ upper confidence level of the line fluxes derived from RGS2 lie well within the 1σ confidence interval of the corresponding line fluxes derived from RGS1 data. The 1σ upper limit on N VI ($x+y$) line is $1.2 \times 10^{-5} \text{ photons cm}^{-2} \text{ s}^{-1}$ and (w) line is $2 \times 10^{-5} \text{ photons cm}^{-2} \text{ s}^{-1}$ obtained from RGS2, while the corresponding line flux obtained from RGS1 fit are $1.9^{+3.3}_{-1.9} \times 10^{-5} \text{ photons cm}^{-2} \text{ s}^{-1}$ and $4.8^{+6}_{-4.2} \times 10^{-5} \text{ photons cm}^{-2} \text{ s}^{-1}$, respectively. Also we find that the lines are blue-shifted relative to their rest wavelength. The resonant lines of both the triplets arise from a cloud in outflow with a high velocity ($v \sim 5000 \text{ km s}^{-1}$). While the outflow velocities of the other two lines, ($x+y$) and z , of the triplets are very low. The velocities are measured with respect to the systemic velocity. We checked statistically whether we detect two distinct outflow velocities or whether one velocity can describe all the line shifts. We tied the redshift of the O VII resonant line in the Gaussian model with the other two lines of the triplet and found that the C statistic worsened by $\Delta C = +8$ from the fit where the resonant line was in a faster outflow.

The detection of the O VII resonant line, which shows the signature of a very high outflow velocity, is weak

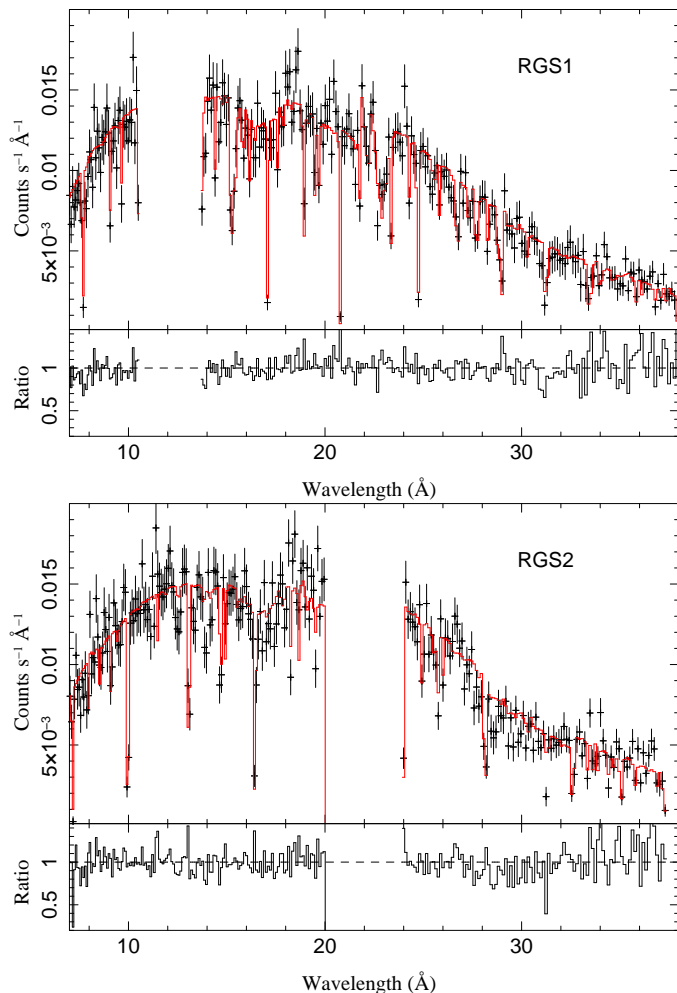


FIG. 2.— Shows the data with the best fit models for RGS1 and RGS2 along with the residuals.

($\Delta C \sim 12$) as inferred from the Gaussian fit. We therefore performed Monte Carlo simulation for more rigorous test of the significance of the line. We used the *ISIS fakeit* command to create 500 fake RGS1 and RGS2 data sets using the best-fit model parameters of the actual dataset. The faked data sets include source+background counts. We fitted the fake data using the same model with background properly subtracted and obtained the best fit Gaussian line parameters of O VII(r) line. These parameter values (line energy and strength) were distributed around their initial or the true values (the value used to simulate the data). The true value and the error at the 90% confidence level on the line energy distribution is 0.5669 keV and 0.001 keV, respectively, and for the line norm distribution is 3.86×10^{-5} photons $\text{cm}^{-2} \text{s}^{-1}$ and 2×10^{-5} photons $\text{cm}^{-2} \text{s}^{-1}$ respectively. The confidence range of detection is comparable to the confidence range obtained using the C-statistic. Thus we detect the resonance line at a 2σ level. The detection of O VII intercombination and forbidden lines at similar significance at appropriate wavelengths suggests that these lines are highly unlikely to be spurious and we consider them as real features.

These He-like X-ray lines are of particular interest since their ratios are used as plasma diagnostics. The Gaussian fit of these lines for both the triplets clearly indicates that the resonant line flux is comparable to the forbidden line flux within the errors (see Table 1). Since the lines apparently arise from clouds having different outflow velocities, it is physically not meaningful to calculate the line ratios. The He-like emission line diagnostics (R and G ratios) enumerated in Gabriel & Jordan (1973) are based on the assumption that all the three lines of the triplet arise from the same cloud. The picture emerging in the case of Mrk 704 is that there are two distinct clouds where each cloud has its own predominating emission lines. We investigate the origin of these lines in more detail with CLOUDY modeling in the next section.

Apart from the two triplets we also detected C VI Lyman α but at a lower significance. The outflow velocity calculated from the line is same as that from resonant lines ($\sim 5000 \text{ km s}^{-1}$).

As suggested by Netzer (1993) the warm absorbing clouds also emit. It is likely that there is a distribution of photoionised, warm clouds in all directions and the clouds along our line of sight give rise to the warm absorption while the clouds in all directions contribute to the emission lines. Thus, it is important to model both warm absorption and warm emission with a distribution of photoionised clouds. Hence we created a table model for warm emission using CLOUDY with the same input continuum used to model the warm absorbers. The electron density of the cloud assumed is 10^9 cm^{-3} .

Addition of a single warm emission component improved the fit by $\Delta C = 26$ for 4 additional parameters compared to the previous two component warm absorber model. We found that only the intercombination and forbidden lines of O VII triplet with similar outflow velocities (inferred from the Gaussian fit) are well fitted while the high velocity resonant lines are not well described. From the study of line ratios of He like triplets, Porquet & Dubau (2000) have shown that a weaker forbidden line is indicative of an emission from a high temperature and high density plasma. So we created another warm emission model using CLOUDY with a higher density $\sim 10^{13} \text{ cm}^{-3}$ and used it to model the faster outflowing resonant lines of the triplets of Mrk 704 which have no forbidden line counterpart. The high density warm emission component fitted the resonant line of O VII and improved the fit by $\Delta C = 31$ for 4 extra parameters ($C/\text{dof} = 3287/3382$). The best-fit parameters are: for the first component $\log \xi = 1.04_{-0.12}^{+0.4}$ and $N_{\text{H}}^{\text{WE}} = 3.9 \pm 0.1 \times 10^{20} \text{ cm}^{-2}$, and outflow velocity $v = -30 \pm 300 \text{ km s}^{-1}$; for the second component $\log \xi = 1.14_{-0.4}^{+0.009}$ and $N_{\text{H}}^{\text{WE}} = 1.0_{-0.1}^{+0.007} \times 10^{18} \text{ cm}^{-2}$ and outflow velocity $v = 5190_{-300}^{+300} \text{ km s}^{-1}$ (The best fit parameters are listed as model 1 in Table 2). The combined best fit-model as well as data for individual RGS instruments are plotted in figure 2.

Another possible scenario could be that we are not detecting the resonant line at all. It may be that a higher velocity outflowing cloud emits intercombination and forbidden lines which exactly coincides with the wavelength of the resonant and intercombination lines of the lower outflow velocity cloud. This possibility is supported by the fact that the energy differences between

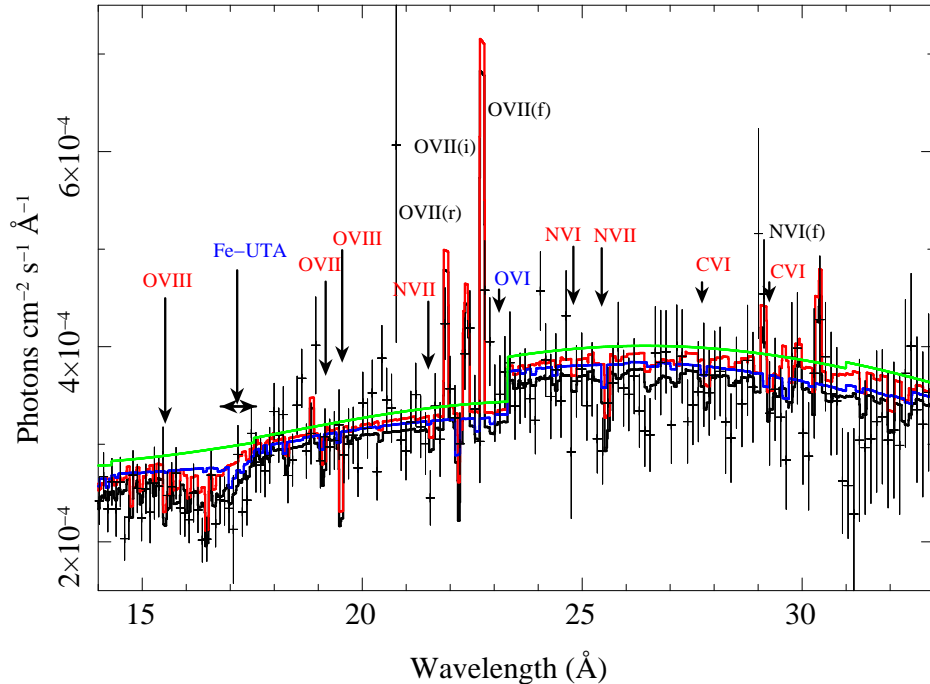


FIG. 3.— The warm absorber model components obtained using Cloudy to jointly fit the RGS1 and RGS 2 data. The data had been grouped by a factor of 10 only for plotting purpose. For clarity we have shown only the RGS1 data. The green line indicates the continuum modified with Galactic absorption as well as the partially covering neutral absorber intrinsic to the source. The red line indicates the continuum modified by the higher ionisation phase of warm absorption $\log \xi = 2.70$ apart from the Galactic absorption which models the O VIII, O VII, N VI, N VII, C VI etc. The blue line indicates the continuum modified by the lower ionisation phase $\log \xi = 1.27$ apart from Galactic absorption which fits the Fe M-shell UTA and OVI. The black line indicates the combined best fit. The emission lines are labelled in black letters.

($x+y$), w and z lines are almost the same (0.006 keV) within the errors (± 0.001 keV). So keeping this in mind we tried to fit the line triplets using the same lower density ($\sim 10^9 \text{ cm}^{-3}$) model, so that the forbidden lines are not suppressed. We used a second warm emission component of similar density ($\sim 10^9 \text{ cm}^{-3}$) instead of the higher density model used in the previous fit. This improved the fit by $\Delta C = 29$ for 4 extra parameters ($C/\text{dof} = 3310/3380$) from the previous fit with a single warm emission component. The best-fit parameters of the second warm emitter component are : $\log \xi = 1.00^{+0.003}_{-0.05}$, $N_{\text{H}}^{\text{WE}} = 2.8^{+0.09}_{-0.5} \times 10^{18} \text{ cm}^{-2}$ and outflow velocity $5000^{+300}_{-300} \text{ km s}^{-1}$, where ξ is expressed in units of erg cm s^{-1} (The best fit parameters are tabulated under model 2 in Table 2). The possible scenarios emerging from these analysis will be discussed in the next section.

4. DISCUSSION

The EPIC-pn spectrum above 2 keV is well described by an absorbed power-law with $\Gamma \sim 1.86$, which is typical of Seyfert 1 galaxies. Apart from Galactic absorption we detected an intrinsic cold absorber that covers the central X-ray source partially with a covering fraction of ≈ 0.22 . The low covering fraction is expected since the soft excess in the EPIC-pn spectrum is prominent and not altered significantly. The high column density ($N_{\text{H}} \sim 10^{23} \text{ cm}^{-2}$) of the partial covering absorber is suggestive of the fact that the cold absorption arises from the torus. This fits well with the picture that Mrk 704 is a polar scattered seiyfert galaxy and hence the viewing

angle is grazing the torus. The angular size of the central X-ray source as seen from the torus is likely ~ 0.3 deg assuming a size of $\sim 50R_{\text{S}}$ for the central X-ray source and ~ 0.1 parsec for the torus. Thus the extended source can be covered partially by the torus.

There is a presence of a broad Fe-K α line at 6.4 keV with an FWHM of ~ 0.23 keV corresponding to $v_{\text{FWHM}} \approx 11000 \text{ km s}^{-1}$. Hence the line can arise either from an accretion disk or inner broad line region. The diskline model fit also suggests that the line arises from regions away from the inner accretion disk ($R = 10 - 20000r_g$).

The soft X-ray region 0.3-2 keV shows the presence of huge soft excess over the power-law. The soft excess emission is described by two black-body components with temperatures, $kT_{\text{BB}} = 0.085$ and 0.22 keV. The soft excess emission contributes $\sim 25\%$ to the 0.3 – 10 keV unabsorbed luminosity of $5.0^{+0.11}_{-0.06} \times 10^{42} \text{ erg s}^{-1}$. All these features indicate that we are directly observing the emission from the central AGN engine.

We estimated the bolometric luminosity L_{bol} from the monochromatic luminosity $L_{\lambda}(5100\text{\AA}) = 4.9 \times 10^{39} \text{ erg s}^{-1} \text{\AA}^{-1}$ (Peterson et al. 1998) and using the relation in Kaspi et al. (2000b),

$$L_{\text{bol}} = 9\lambda L_{\lambda}(5000\text{\AA}), \quad (2)$$

which gives $L_{\text{bol}} = 2.2 \times 10^{44} \text{ erg s}^{-1}$. Thus $\sim 2.3\%$ of the bolometric luminosity is emitted in the X-ray band of 0.3 – 10 keV. The corresponding Eddington ratio can be obtained as $\lambda_{\text{Edd}} = \frac{L_{\text{bol}}}{L_{\text{Edd}}} = 0.016$, where

TABLE 2

BEST-FIT MODEL PARAMETERS DERIVED FROM THE SIMULTANEOUS FIT OF HIGH RESOLUTION RGS 1 AND RGS 2 OBSERVATION OF MRK-704(USING CLOUDY)

Model components	parameters	Model 1 ^a		Model 2 ^b	
Neutral absorption	N_H (10^{20} cm ⁻²)	2.97		2.97	
Intrinsic neutral absorption	N_H (10^{22} cm ⁻²) Covering fraction	50 0.22		50 0.22	
Power law	Γ $norm_{PL}$	1.865 $(4.5 \pm 0.01) \times 10^{-3}$		1.865 $(4.5 \pm 0.01) \times 10^{-3}$	
Blackbody	kT_{in} (eV) $norm$	83.5^{+2}_{-1} $1.4^{+0.7}_{-0.5} \times 10^{-4}$		83.5^{+2}_{-1} $1.4^{+0.7}_{-0.5} \times 10^{-4}$	
Warm absorber I	N_H^{WA} (10^{20} cm ⁻²) $\log \xi$ $(v/$ km s ⁻¹) ^d z	$2.69^{+1.11}_{-0.75}$ $2.7^{+0.3}_{-0.15}$ -540 ± 100 0.0274 ± 0.0004	$\Delta C = 106^c$	$2.69^{+1.11}_{-0.75}$ $2.7^{+0.3}_{-0.15}$ -540 ± 100 0.0274 ± 0.0004	$\Delta C = 106$
Warm absorber II	N_H^{WA} (10^{20} cm ⁻²) $\log \xi$ $(v/$ km s ⁻¹) z	$2^{+0.5}_{-0.5}$ $1.27^{+0.27}_{-0.52}$ -1350 ± 300 0.0245 ± 0.001	$\Delta C = 12$	$2^{+0.5}_{-0.5}$ $1.27^{+0.27}_{-0.52}$ -1350 ± 300 0.0245 ± 0.001	$\Delta C = 12$
Warm emitter I	N_H^{WE} (10^{20} cm ⁻²) $\log \xi$ $(v/$ km s ⁻¹) z $norm$	3.9 ± 0.1 $1.04^{+0.4}_{-0.12}$ -30 ± 300 $0.0289^{+0.0012}_{-0.002}$ $(5.3 \pm 2.5) \times 10^{-19}$	$\Delta C = 26$	3.9 ± 0.1 $1.04^{+0.4}_{-0.12}$ -30 ± 300 $0.0289^{+0.0012}_{-0.002}$ $(5.3 \pm 2.5) \times 10^{-19}$	$\Delta C = 26$
Warm emitter II	N_H^{WE} (cm ⁻²) $\log \xi$ $(v/$ km s ⁻¹) z $norm$	$1.00^{+0.007}_{-0.11} \times 10^{18}$ $1.14^{+0.009}_{-0.40}$ -5190 ± 300 0.0119 ± 0.001 $8.7^{+0.05}_{-0.4} \times 10^{-17}$	$\Delta C^* = 31$	$2.8^{+0.5}_{-0.09} \times 10^{18}$ $1.00^{+0.003}_{-0.05}$ -5490 ± 300 0.0109 ± 0.001 $1.57^{+0.05}_{-0.4} \times 10^{-19}$	$\Delta C = 29$
C/dof		3287/3382		3289/3382	

^aThis model is $wabs \times cold\ absorber \times warmabsorber(1) \times warmabsorber(2) \times (powerlaw + bbody + warmemitter(1) + warmemitter(2))$, where the second warm emitter has a higher density ($n_e = 10^{13}$ cm⁻³).

^bThis model is same as above, except the second warm emitter has same density ($n_e = 10^9$ cm⁻³)

^cThe Reduction in C quoted as ΔC besides each model component indicates the improvement in statistics from its existing value on addition of that model.

^dOutflow velocity.

$L_{Edd} = 1.38 \times 10^{38} \frac{M_{BH}}{M_{\odot}} = 1.13 \times 10^{46}$ erg s⁻¹, with black-hole mass, $M_{BH} = 8.2 \times 10^7 M_{\odot}$ estimated from the reverberation relation (see below).

4.1. The warm absorbers

We have found significant absorption of the soft X-ray emission by partially ionised medium in Mrk 704. We have constrained the warm absorption in Mrk 704 to consist of two strong absorber components as is the case in other Seyfert 1 galaxies e.g., IRAS 13349+2438 (Sako et al. 2001), NGC 3783 (Krongold et al. 2003), Mrk 841 (Longinotti et al. 2010). The lower ionisation phase ($\log \xi = 1.27$) contributes to the Fe M shell UTA and O VI, while the higher ionisation phase ($\log \xi = 2.7$) gives rise to the absorption from O VII, O VIII, N VI, N VII, and C VI (see Fig. 3). The broad range of charge states observed along the line of sight is typical of Seyfert outflows (Behar et al. 2003).

The lower ionisation phase is found in outflow with a

velocity of ~ 1350 km s⁻¹, while the higher ionisation phase has a lower outflow velocity of ~ 540 km s⁻¹. The picture is consistent with a radiatively driven outflow, where the lower ionisation phase has a greater optical depth for the ionising radiation and hence the cloud acquires more momentum from the ionising flux than the higher ionisation phase. Another possible explanation is that the high velocity, low ionisation component originates closer to the nucleus where the escape velocity is very high, and the high ionisation component could be launched much further away. In keeping with the Polar scattered Seyfert scenario it is tempting to think of the higher ionisation (lower velocity) phase to emanate from the torus (torus wind). However this is unlikely since for such a highly photoionised plasma to exist at such a large distance from the nucleus, the corresponding density of the cloud has to be very low.

4.1.1. Energetics of Warm absorbers

TABLE 3
DETAILS OF THE CALCULATED WARM ABSORBER PARAMETERS OF MRK 704

Calculated parameters	W.A component 1 (log $\xi=2.7$)	W.A component 2 (log $\xi=1.27$)	Units
outflow velocity	540 ± 100	1350 ± 300	km s^{-1}
r_{min}	$R > 10^{-3}$	$R > 2 \times 10^{-3}$	pc
r_{max}	$R < 100$	$R < 10^3$	pc
Volume filling factor(C_v)	3.81×10^{-3}	2×10^{-5}	–
Mass outflow rate	2.5×10^{-5}	5.0×10^{-4}	$M_{\odot} \text{ yr}^{-1}$
$\frac{L_{\text{KE}}}{L_{\text{ion}}}$	10^{-6}	10^{-5}	–
Width along LOS($\Delta R = \frac{N_{\text{H}}}{n_{\text{e}}}$)	3×10^{11}	5×10^{11}	cm

r_{min} and r_{max} are the minimum and maximum distance of the clouds from the central engine.

As in many Seyfert 1 galaxies, the warm absorbers in Mrk 704 are in outflow. The associated mass outflow rate can be estimated by assuming that the warm absorber is in the form of spherical outflow with the gas density smoothly decreasing as $1/r^2$ and with a uniform volume filling factor C_v . Following Blustin et al. (2005), the mass outflow rate can be written as

$$\dot{M}_{\text{out}} \sim \frac{1.23m_p L_{\text{ion}} C_v v \Omega}{\xi}, \quad (3)$$

where L_{ion} is the ionizing luminosity, v is outflow velocity and Ω is the solid angle subtended by the outflow. The covering fraction is given by

$$C_v \sim \frac{(L_{\text{abs}} + L_{\text{ion}}(1 - e^{-\tau}))\xi}{1.23m_p c L_{\text{ion}} \Omega v^2}, \quad (4)$$

where τ is the Thomson scattering optical depth and L_{abs} is the luminosity absorbed by the cloud in the whole energy band of 0.3 – 10 keV.

We have calculated L_{abs} for the two warm absorber phases from the best-fitting models to the RGS data. The luminosity absorbed by the higher and lower ionisation phases is $L_{\text{abs}} = 1 \times 10^{41} \text{ erg s}^{-1}$ and $4.0 \times 10^{41} \text{ erg s}^{-1}$ respectively, in the 0.3 – 10 keV band. We calculated the ionising luminosity as the unabsorbed luminosity in 0.3 – 10keV band, and the Thomson scattering optical depth using the best-fit absorption columns to be $\tau \sim 1.7 \times 10^{-4}$ and $\sim 1.3 \times 10^{-4}$, respectively, for the higher and lower ionisation components. Using the above values and Eqn. 4, we obtained volume filling factors C_v of $\sim 4.8 \times 10^{-3}$ and $\sim 4.8 \times 10^{-4}$ for the higher ionisation and lower ionisation phases, respectively. We have used the outflow velocities derived from the best-fitting warm absorber model to RGS data. Using Eqn. 3, we estimate the mass outflow rate, $\dot{M}_{\text{out}} \sim 2.5 \times 10^{-5} M_{\odot} \text{ yr}^{-1}$ for the high ionisation phase and $\dot{M}_{\text{out}} \sim 5.0 \times 10^{-4} M_{\odot} \text{ yr}^{-1}$ for the low ionisation phase.

We used $\Omega \sim 1.5$, typical for Seyfert 1s Blustin et al. (2005). The results are listed in Table 3. For compari-

son, we have also estimated the mass accretion rate for Mrk 704 as

$$\dot{M}_{\text{acc}} = \frac{L_{\text{bol}}}{\eta c^2}, \quad (5)$$

where we assumed the accretion efficiency $\eta = 0.1$. The mass accretion rate thus estimated is $\dot{M}_{\text{acc}} = 0.038 M_{\odot} \text{ yr}^{-1}$. Thus the total mass outflow rate in the warm absorbers is 13% of the mass accretion rate.

4.1.2. Location of the warm absorbers

The maximum distance of the warm absorbing clouds can be estimated using the argument that the size of the cloud ΔR is very less than its distance from the source R . In that case using the expression $\xi = L/nR^2$ we have

$$\frac{\xi R N_{\text{H}}}{L} < 1, \quad (6)$$

which gives $R < 100 \text{ pc}$ and $R < 10^4 \text{ pc}$ for the high ionisation and low ionisation components respectively. The minimum distance of the cloud can be estimated by noting that its outflow velocity must be greater than or equal to the escape velocity at that radius.

$$\frac{GM}{R} < \frac{v^2}{2}, \quad (7)$$

From this we get $R > 10^{-1} \text{ pc}$ and $R > 10^{-3} \text{ pc}$ for the high ionisation and low ionisation components respectively. Recently Stoll et al. (2009) and Krongold et al. (2007) have considered more realistic approaches to constrain the warm absorber distances.

The mass of the central blackhole was calculated using an empirical relation obtained by Kaspi et al. (2000b) using the reverberation techniques,

$$M = 1.464 \times 10^5 \left[\frac{R_{\text{BLR}}}{\text{lt} - \text{days}} \right] \left[\frac{v_{\text{FWHM}}}{10^3 \text{ km s}^{-1}} \right]^2 M_{\odot}, \quad (8)$$

$$R_{BLR} = (32.9^{+2.0}_{-1.9}) \left[\frac{\lambda L_{\lambda}(5100\text{\AA})}{10^{44} \text{ erg s}^{-1}} \right]^{0.700 \pm 0.03} \text{ lt - days}, \quad (9)$$

where R_{BLR} is the distance of the broad line region from the central engine which is estimated in terms of time lags in Balmer emission lines. v_{FWHM} is the velocity broadening of the Balmer lines assuming that the line widths represent a Keplerian velocity. The value of $\lambda L_{\lambda}(5100\text{\AA})$ in case of Mrk 704 was obtained from previous optical studies by Peterson et al. (1998). The v_{FWHM} of the H_{α} line is $\sim 6750 \text{ km s}^{-1}$ and was obtained from the paper Moore et al. (1996). The estimated mass turns out to be $\sim 8.2 \times 10^7 M_{\odot}$.

4.2. The warm emitters

Apart from warm absorption, we detected emission features arising from He-like ions of O and N and H-like ion of C. Simple Gaussian profile fits suggested that the resonance lines are significantly blueshifted by $v \sim 5000 \text{ km s}^{-1}$ relative to the forbidden and intercombination lines. This is possible if two sets of kinematically distinct clouds contribute to the emission line triplets such that resonance lines predominantly arise from high velocity clouds while the forbidden and intercombination lines arise from the low velocity clouds. The forbidden lines from the high velocity clouds can be suppressed if the density is high or the UV radiation field is intense. The density dependence arises as the 3S_1 level electrons can be collisionally excited to the 3P levels. At sufficiently high density, more than the critical density for the forbidden line ($\approx 3 \times 10^{10} \text{ cm}^{-3}$ for O VII, (Ness et al. 2001)), the collisional excitation from $^3S_1 \rightarrow ^3P$ weakens the forbidden line.

The He-like line ratios can also be altered by the presence of UV radiation (Gabriel & Jordan 1969). If the photon flux is high at the wavelength corresponding to the energy difference between forbidden and intercombination line levels, i.e 1900Å for N VI and 1630Å for O VII (6.5 eV and 7.6 eV respectively), the 3S_1 level can be photoexcited to the 3P levels. The more the photon flux at these energies, the more is the forbidden level depleted to intercombination level ($2 S^3 \rightarrow 2 P^3$). Thus the forbidden line becomes weaker and the intercombination lines stronger.

In keeping with the polar scattered Seyfert scenario we can say that the clouds that are in the shadow of the torus face a weaker UV flux and hence emit predominantly forbidden and intercombination lines. They are also of lower densities. But the higher density clouds facing the central engine have their forbidden lines suppressed and have prominent resonant lines.

The widths of the emission lines are $\leq 700 \text{ km s}^{-1}$, similar to the emission lines observed from optical narrow-line region (NLR). The density in the NLR is typically $n_e \sim 10^3 - 10^4 \text{ cm}^{-3}$. At these densities (i.e below the critical densities) the forbidden lines of O VII are expected to be strong (Kinkhabwala et al. 2002). Thus, it is possible that the forbidden and intercombination lines arise from the optical NLR. The high-velocity resonance lines arise from a more dense region nearer the central engine.

Another possibility is that we do not really detect the

resonance lines but detect the intercombination and the forbidden lines. If one set of emission lines is blueshifted such that the intercombination line of the low velocity cloud coincides with the forbidden line of the high velocity cloud, then the overall line structure will be triplet - the forbidden line from the low velocity cloud (0.545 keV), the blended intercombination line from the low velocity cloud and the forbidden line from the high velocity cloud (0.553 keV), and the intercombination line from the high velocity cloud (0.5669 keV). The energy difference between those lines (x+y), w and z are similar within the errors and hence this overlapping is a possibility. In this case, emission lines from two low density clouds with different outflow velocities describe the observed triplet lines. However, this model over predicts the central intercombination line (see Fig 4, panel c) and is marginally statistically poorer than the previous high density fit.

However, there are a few caveats in our analysis. Emission from any cloud is almost an isotropic process and the viewing solid angle subtended at our eye by these clouds being very less, the emission features are mostly very weak. Also the emission features are contributed from all clouds distributed around the source unlike the absorbers which lie only along our line of sight to the source. So the physical conditions in such emitting clouds are varied and complex. Hence fitting the emission lines by discrete parameter values may not give us a clear picture. As pointed out by Kinkhabwala et al. (2002), the emission features could be modelled by a continuous distribution of ξ and N_H as against our discrete cloud assumption. Each cloud with different physical conditions might be contributing little to the spectrum and what we see is the sum of the effect of all such clouds. The electron densities n_e assumed while modelling with Cloudy were 10^9 cm^{-3} and 10^{13} cm^{-3} which might not be appropriate for clouds with widely varying conditions.

The observations of the emission lines from this type 1 AGN is likely due to the reduced X-ray continuum by the partial covering neutral absorber as revealed in the EPIC-pn data and earlier by *ASCA* and *Swift* observations (see Ajello et al. 2008). This implies that the cold partial covering absorber is closer to the nuclear X-ray source than the X-ray line emitting region. If the cold absorption is provided by the torus, then the X-ray line emitting region must be outside this torus. This suggests that the low velocity X-ray line emitting region is similar to the X-ray narrow line region observed from Seyfert 2 galaxies such as NGC 1068 (Kinkhabwala et al. 2002)

5. CONCLUSION

We have performed a detailed analysis of a long *XMM-Newton* observation of Mrk 704. The main results are as follows:

1. The 0.3-10 keV continuum is well described by a power-law with slope $\Gamma \sim 1.865$ and a soft X-ray excess component consisting of two black-bodies with temperatures $kT \approx 0.085$ and 0.22 keV . The soft excess contributes $\sim 25\%$ to the $0.3 - 10 \text{ keV}$ intrinsic flux.
2. We detected the presence of a partially covering cold absorber intrinsic to the source. The high col-

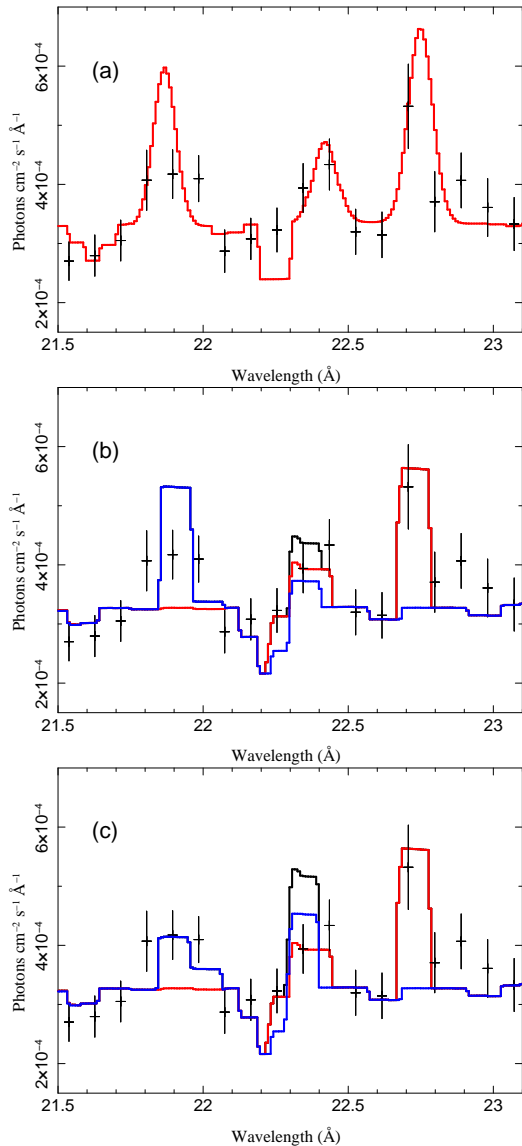


FIG. 4.— Shows the modelled O VII emission lines. The panel (a) shows Gaussian fit to the three lines. The panel (b) shows the fit using two warm emission models created using CLOUDY. One is created using a cloud density of 10^{13} cm^{-3} and the other using a density 10^9 cm^{-3} . The blue line shows the higher density model for the faster outflowing resonant line while the red line shows the lower density model for the forbidden and intercombination lines. The panel (c) shows the fit using the emission line models created using a cloud density of 10^9 cm^{-3} . The blue line models the faster outflowing emission lines while the red line models the lower velocity cloud emission lines. In the panels (b) and (c) the black line shows the combined best fit.

umn density ($N_H \sim 10^{23} \text{ cm}^{-2}$) of the cold absorber supports the fact that Mrk 704 is a polar scattered Seyfert galaxy and we are looking at the source along a line of sight that grazes the torus.

3. A broad FeK α line is detected at 6.4 keV with $v_{\text{FWHM}} \approx 11000 \text{ km s}^{-1}$. The line can arise either from the inner broad line region or the outer regions of the accretion disk.
4. A two phase warm absorber with $\log \xi \approx 1.27$ and $\log \xi \approx 2.7$ is detected in the spectra. The lower ionisation phase has a faster outflow velocity $\sim 1350 \text{ km s}^{-1}$ while the higher ionisation phase has a lower velocity $\sim 450 \text{ km s}^{-1}$.
5. Weak emission features of He-like triplets of O VII and N VI are identified. One of the lines in the triplets is in much faster outflow ($\sim 5000 \text{ km s}^{-1}$) than the other two lines which are from a cloud with outflow velocity consistent with zero. The CLOUDY modelling points out to two possible situations. The first is that there are two sets of clouds with two different velocities and two different densities ($n = 10^9$ and 10^{13} cm^{-3}). The higher density, higher outflow velocity cloud produces the resonant line while the lower density lower velocity cloud gives rise to the intercombination and forbidden lines. The second situation is that there are two clouds of low density ($n = 10^9 \text{ cm}^{-3}$) but with different outflow velocities giving only intercombination and forbidden lines.
6. The low density emission phase is likely similar to the X-ray narrow-line region observed from many Seyfert 2 galaxies. The high velocity, outflowing emission phase is unique to Mrk 704.

Acknowledgements : We thank an anonymous referee for his/her insightful comments and suggestions. We also thank Smita Mathur, Matteo Guainazzi for useful discussions and comments on the paper. We are also thankful to Gary Ferland and Ryan Porter for discussions on the CLOUDY modeling. One of the authors SL is grateful to CSIR, Government of India for supporting this work.

REFERENCES

- Ajello, M., et al. 2008, ApJ, 673, 96
 Behar, E., Rasmussen, A. P., Blustin, A. J., Sako, M., Kahn, S. M., Kaastra, J. S., Branduardi-Raymont, G., & Steenbrugge, K. C. 2003, ApJ, 598, 232
 Blustin, A. J., Page, M. J., Fuerst, S. V., Branduardi-Raymont, G., & Ashton, C. E. 2005, A&A, 431, 111
 Braito, V., et al. 2007, ApJ, 670, 978
 Cash, W. 1979, ApJ, 228, 939
 Dadina, M., & Cappi, M. 2004, A&A, 413, 921
 Dasgupta, S., Rao, A. R., Dewangan, G. C., & Agrawal, V. K. 2005, ApJ, 618, L87
 Dewangan, G. C., Griffiths, R. E., Dasgupta, S., & Rao, A. R. 2007, ApJ, 671, 1284
 Elvis, M., et al. 1994, ApJS, 95, 1
 Fabian, A. C., Crawford, C. S., & Iwasawa, K. 2002, MNRAS, 331, L57
 Ferland, G. J., Korista, K. T., Verner, D. A., Ferguson, J. W., Kingdon, J. B., & Verner, E. M. 1998, PASP, 110, 761
 Gabriel, A. H., & Jordan, C. 1969, Nature, 221, 947
 —. 1973, ApJ, 186, 327
 George, I. M., Turner, T. J., Netzer, H., Nandra, K., Mushotzky, R. F., & Yaqoob, T. 1998, ApJS, 114, 73
 Gierliński, M., & Done, C. 2004, MNRAS, 349, L7
 Halpern, J. P. 1984, ApJ, 281, 90

- Jiménez-Bailón, E., Guainazzi, M., Matt, G., Bianchi, S., Krongold, Y., Piconcelli, E., Santos Lleó, M., & Schartel, N. 2008, in *Revista Mexicana de Astronomía y Astrofísica Conference Series*, Vol. 32, *Revista Mexicana de Astronomía y Astrofísica Conference Series*, 131–133
- Kaasra, J. S., Mewe, R., Liedahl, D. A., Komossa, S., & Brinkman, A. C. 2000, *A&A*, 354, L83
- Kalberla, P. M. W., Burton, W. B., Hartmann, D., Arnal, E. M., Bajaja, E., Morras, R., & Pöppel, W. G. L. 2005, *A&A*, 440, 775
- Kaspi, S., Brandt, W. N., Netzer, H., Sambruna, R., Chartas, G., Garmire, G. P., & Nousek, J. A. 2000a, *ApJ*, 535, L17
- Kaspi, S., Smith, P. S., Netzer, H., Maoz, D., Jannuzi, B. T., & Giveon, U. 2000b, *ApJ*, 533, 631
- Kinkhabwala, A., et al. 2002, *ArXiv Astrophysics e-prints*
- Krongold, Y., Nicastro, F., Brickhouse, N. S., Elvis, M., Liedahl, D. A., & Mathur, S. 2003, *ApJ*, 597, 832
- Krongold, Y., Nicastro, F., Elvis, M., Brickhouse, N., Binette, L., Mathur, S., & Jiménez-Bailón, E. 2007, *ApJ*, 659, 1022
- Longinotti, A. L., Nucita, A., Santos-Lleo, M., & Guainazzi, M. 2008, *A&A*, 484, 311
- Longinotti, A. L., et al. 2010, *A&A*, 510, A92+
- Magdziarz, P., Blaes, O. M., Zdziarski, A. A., Johnson, W. N., & Smith, D. A. 1998, *MNRAS*, 301, 179
- Mathur, S., Elvis, M., & Wilkes, B. 1995, in *Bulletin of the American Astronomical Society*, Vol. 27, *Bulletin of the American Astronomical Society*, 875–+
- Moore, D., Cohen, R. D., & Marcy, G. W. 1996, *ApJ*, 470, 280
- Nandra, K., & Pounds, K. A. 1994, *MNRAS*, 268, 405
- Ness, J., et al. 2001, *A&A*, 367, 282
- Netzer, H. 1993, *ApJ*, 411, 594
- Nucita, A. A., Guainazzi, M., Longinotti, A. L., Santos-Lleo, M., Maruccia, Y., & Bianchi, S. 2010, *A&A*, 515, A47+
- Peterson, B. M., Wanders, I., Bertram, R., Hunley, J. F., Pogge, R. W., & Wagner, R. M. 1998, *ApJ*, 501, 82
- Piconcelli, E., Jimenez-Bailón, E., Guainazzi, M., Schartel, N., Rodríguez-Pascual, P. M., & Santos-Lleó, M. 2005, *A&A*, 432, 15
- Porquet, D., & Dubau, J. 2000, *A&AS*, 143, 495
- Porter, R. L., Ferland, G. J., Kraemer, S. B., Armentrout, B. K., Arnaud, K. A., & Turner, T. J. 2006, *PASP*, 118, 920
- Pounds, K. A., Reeves, J. N., King, A. R., & Page, K. L. 2004, *MNRAS*, 350, 10
- Reeves, J. N., O'Brien, P. T., & Ward, M. J. 2003, *ApJ*, 593, L65
- Reynolds, C. S. 1997, in *Astronomical Society of the Pacific Conference Series*, Vol. 128, *Mass Ejection from Active Galactic Nuclei*, ed. N. Arav, I. Shlosman, & R. J. Weymann, 173–+
- Sako, M., et al. 2001, *A&A*, 365, L168
- Schwope, A., et al. 2000, *Astronomische Nachrichten*, 321, 1
- Smith, J. E., Robinson, A., Alexander, D. M., Young, S., Axon, D. J., & Corbett, E. A. 2004, *MNRAS*, 350, 140
- Smith, J. E., Young, S., Robinson, A., Corbett, E. A., Giannuzzo, M. E., Axon, D. J., & Hough, J. H. 2002, *MNRAS*, 335, 773
- Stoll, R., Mathur, S., Krongold, Y., & Nicastro, F. 2009, *ArXiv e-prints*
- Tananbaum, H., et al. 1979, *ApJ*, 234, L9
- Young, M., Elvis, M., Risaliti, G., & Marscher, A. 2009, in *Bulletin of the American Astronomical Society*, Vol. 41, *Bulletin of the American Astronomical Society*, 454–+
- Zamorani, G., et al. 1981, *ApJ*, 245, 357

TABLE 4
IMPROVEMENT IN STATISTICS ON ADDITION OF A MODEL AS DERIVED FROM THE MEDIUM RESOLUTION EPIC-PN DATA ANALYSIS OF MRK-704

Models ^d	PL ^a (Γ)	wabs ^a $N_{\text{H}}^{\text{Gal}}$ (10^{20} cm^{-2})	PCA ^a $N_{\text{H}}^{\text{PCA}}$ (10^{23} cm^{-2}) C_{v}	$\text{GL}_{\text{FeK}\alpha}$ ^a E, σ Flux ^e	BB(1) ^a kT (keV)	BB(2) ^a kT (keV)	WA(1) ^a N_{H}^{WA} (10^{21} cm^{-2}) $\log \frac{\xi}{\text{erg cm s}^{-1}}$	WA(2) ^a N_{H}^{WA} (10^{20} cm^{-2}) $\log \frac{\xi}{\text{erg cm s}^{-1}}$	GL E, σ Flux ^e	χ^2/dof
Model 1 ^b	1.76	2.97	–	–	–	–	–	–	–	361/219
Model 2 ^b	1.88	2.97	4.4	–	–	–	–	–	–	297/217
Model 3 ^b	1.88	2.97	0.31 4.4 0.31	6.39, 0.1 1.7×10^{-5}	–	–	–	–	–	173/214
Model 4 ^c	1.88	2.97	7.0 0.21	6.39, 0.1 1.7×10^{-5}	0.089	–	–	–	–	1259/552
Model 5 ^c	1.88	2.97	6.1 0.21	6.39, 0.1 1.7×10^{-5}	0.089	0.3	–	–	–	876/550
Model 6 ^c	1.85	2.97	5.1 0.31	6.39, 0.1 1.7×10^{-5}	0.088	0.23	1.1 0.99	–	–	606/547
Model 7 ^c	1.865	2.97	5.0 0.22	6.39, 0.1 1.7×10^{-5}	0.085	0.22	0.97 0.84	1.0 2.97	–	570/544
Model 8 ^c (Best fit)	1.865 ± 0.02	2.97	$5_{-0.8}^{+0.7}$ $0.22_{-0.07}^{+0.02}$	$6.39_{-0.03}^{+0.03}, 0.1_{-0.03}^{+0.03}$ $1.7_{-0.7}^{+0.5} \times 10^{-5}$	$0.085_{-0.002}^{+0.002}$	0.22 ± 0.02	$0.97_{-0.17}^{+0.13}$ $0.84_{-0.12}^{+0.25}$	$1_{-0.11}^{+0.4}$ 2.97 ± 0.11	$0.565_{-0.009}^{+0.008}, 0.01_{-0.003}^{+0.002}$ $1.0_{-0.5}^{+0.6} \times 10^{-4}$	559/541

^aPL= Power Law, wabs= Galactic absorption, PCA= partially covering cold absorption, BB= Black Body, WA= Warm absorbers developed using Cloudy, GL=Gaussian line.

^bThese models are in the range 2-10 keV; ^cThese models are in the range 0.3-10 keV

^d Model 1 = wabs \times PL; Model 2 = wabs \times PCA \times PL; Model 3 = wabs \times PCA \times (PL + GL); Model 4 = wabs \times PCA \times (PL + GL + BB)

Model 5 = wabs \times PCA \times (PL + GL + BB(1) + BB(2)); Model 6 = wabs \times PCA \times WA \times (PL + GL + BB(1) + BB(2));

Model 7 = wabs \times PCA \times WA(1) \times WA(2) \times (PL + GL + BB(1) + BB(2)); Model 8 = wabs \times PCA \times WA(1) \times WA(2) \times (PL + GL + BB(1) + BB(2) + GL(2))

^eFluxes are in the units of Photons $\text{cm}^{-2} \text{s}^{-1}$

The observed Luminosities $L_{0.3-10 \text{ keV}} = 4.2_{-0.05}^{+0.05} \times 10^{42} \text{ erg s}^{-1}$, $L_{0.3-2 \text{ keV}} = 2.02_{-0.02}^{+0.04} \times 10^{42} \text{ erg s}^{-1}$, $L_{2-10 \text{ keV}} = 2.18_{-0.02}^{+0.02} \times 10^{42} \text{ erg s}^{-1}$